

The Atmospheric Boundary Layer and the Initiation of the MJO

RICHARD H. JOHNSON^b,^a SIMON P. DE SZOEKE,^b PAUL E. CIESIELSKI,^a AND W. ALAN BREWER^c

^a Colorado State University, Fort Collins, Colorado

^b Oregon State University, Corvallis, Oregon

^c NOAA Chemical Sciences Laboratory, Boulder, Colorado

(Manuscript received 4 April 2023, in final form 9 August 2023, accepted 15 August 2023)

ABSTRACT: The Indian Ocean is a frequent site for the initiation of the Madden–Julian oscillation (MJO). The evolution of convection during MJO initiation is intimately linked to the subcloud atmospheric mixed layer (ML). Much of the air entering developing cumulus clouds passes through the cloud base; hence, the properties of the ML are critical in determining the nature of cloud development. The properties and depth of the ML are influenced by horizontal advection, precipitation-driven cold pools, and vertical motion. To address ML behavior during the initiation of the MJO, data from the 2011/12 Dynamics of the MJO Experiment (DYNAMO) are utilized. Observations from the research vessel *Revelle* are used to document the ML and its modification during the time leading up to the onset phase of the October MJO. The mixed layer depth increased from ~500 to ~700 m during the 1–12 October suppressed period, allowing a greater proportion of boundary layer thermals to reach the lifting condensation level and hence promote cloud growth. The ML heat budget defines an equilibrium mixed layer depth that accurately diagnoses the mixed layer depth over the DYNAMO convectively suppressed period, provided that horizontal advection is included. The advection at the *Revelle* is significantly influenced by low-level convective outflows from the southern ITCZ. The findings also demonstrate a connection between cirrus clouds and their remote impact on ML depth and convective development through a reduction in the ML radiative cooling rate. The emergent behavior of the equilibrium mixed layer has implications for simulating the MJO with models with parameterized cloud and turbulent-scale motions.

KEYWORDS: Boundary layer; Cumulus clouds; Madden-Julian oscillation; Mixed layer

1. Introduction

The 2011/12 Dynamics of the MJO (DYNAMO; Yoneyama et al. 2013; Zhang et al. 2013) field campaign provided an unprecedented array of observations directed at the initiation of the Madden–Julian oscillation (MJO; Madden and Julian 1972). During the months of October and November 2011, two prominent MJOs developed and subsequently moved eastward across the Indian Ocean. These events were associated with global circumnavigating Kelvin waves (Gottschalk et al. 2013; Powell and Houze 2015a; Zhang et al. 2017; Chen and Zhang 2019). Evidence is accumulating to indicate that such planetary Kelvin waves are linked to a large class of MJOs that initiate over the Indian Ocean (Kikuchi and Takayabu 2003; Matthews 2008; Haertel et al. 2015; Powell and Houze 2015a). It is postulated that the Kelvin waves force anomalous lifting, thereby reducing large-scale subsidence and promoting midtropospheric moistening and cloud development during the onset phases of the MJOs (Powell and Houze 2015a; Powell 2016, 2017; Snide et al. 2021).

In addition to global-scale Kelvin waves, localized processes over the Indian Ocean have been found to play a key role in MJO initiation. In large part these processes involve ocean–atmosphere coupling. During periods of suppressed convective activity, insolation warms the upper ocean, resulting in a gradual buildup of convective instability and an increase in shallow cloud populations (Weller and Anderson 1996; Vialard et al. 2009; Johnson and Ciesielski 2013; Moux et al. 2014; Xu and Rutledge 2014; de Szoeke et al. 2015; DeMott et al. 2015). Over time, shallow cumulus evolve into congestus clouds that organize into mesoscale cellular patterns as precipitation-generated cold pools develop (Johnson et al. 1999; Rowe and Houze 2015; Ruppert and Johnson 2015; Powell 2016; de Szoeke et al. 2017; Zuidema et al. 2017). Additionally, diurnal warm layers in the upper ocean during suppressed, light-wind periods serve to accelerate the transition of congestus clouds into deep convection in the onset phase of the MJO (Bellenger et al. 2010; Ruppert 2016; Ruppert and Johnson 2016). The inclusion of the effects of air–sea coupling and diurnal warm layers in numerical simulations of the MJO has yielded improved simulated characteristics of this phenomenon (Bernie et al. 2008; Klingaman and Woolnough 2014; DeMott et al. 2015; Wu et al. 2021).

Corresponding author: Richard H. Johnson, Richard.H.Johnson@colostate.edu

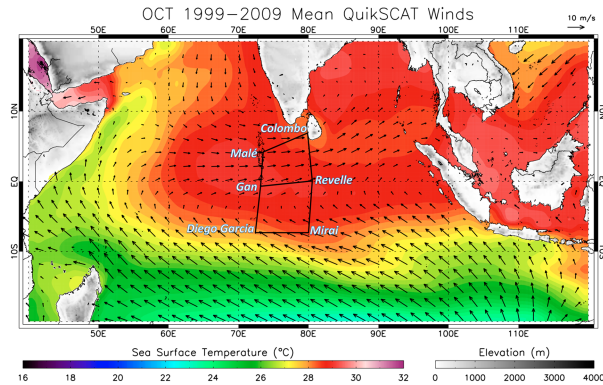


FIG. 1. October 1999–2009 mean SST ($^{\circ}\text{C}$) and QuikSCAT winds. Sounding sites in the DYNAMO northern sounding array and southern sounding array are indicated.

An important aspect of the Indian Ocean related to MJO initiation is the climatological warm pool that spans much of the basin in boreal fall and winter. Figure 1 shows the 11-yr 1999–2009 October mean sea surface temperature and wind field over the Indian Ocean along with the 2011 DYNAMO sounding arrays. Nearly basinwide, southeasterlies flow across strong sea surface temperature (SST) gradients just south of the equator. This flow configuration implies significant atmospheric boundary layer air mass modification. Changes in boundary layer turbulent kinetic energy and hydrostatic pressure across SST gradients can drive low-level convergence, favoring the development of convection (Lindzen and Nigam 1987; Hayes et al. 1989; Wallace et al. 1989). Li and Carbone (2012) showed that low-level convergence or divergence is related to the Laplacian of the SST field. While this concept has been applied to SST gradients of mesoscale dimension, it has also been shown to be relevant to the larger-scale SST distribution over the Indian Ocean and how it influences MJO initiation (Carbone and Li 2015; de Szoeke and Maloney 2020). The air–sea coupling study of Rydbeck et al. (2017) also related low-level convergence to SST gradients in the Indian Ocean warm pool associated with downwelling equatorial oceanic Rossby waves in the eastern Indian Ocean forced by the MJO, which subsequently reemerge in the western Indian Ocean ~ 70 days later. The study by de Szoeke and Maloney (2020) used a simple mixed layer wind model to show that the Indian Ocean SST warm pool acts to increase the moist static energy in the lower troposphere to assist initiation of the MJO.

While SST gradient-driven convergence is an important process for preconditioning the lower-tropospheric environment, cumulus cloud development associated with SST during the MJO initiation phase is mediated through the atmospheric boundary layer. This aspect of MJO initiation is addressed in this paper. The bases of cumulus clouds are near the top of the mixed layer and air ascending through cloud base comes from the mixed layer. Therefore, modification of mixed layer properties by horizontal advection can be expected to affect the nature of the cloud populations that develop. The low-level flow from cold to warm SSTs along 5°S in Fig. 1 leads to a

modification of boundary layer air, enhanced surface buoyancy fluxes, and a deepening atmospheric mixed layer (Schubert et al. 1979; de Szoeke and Bretherton 2004; Small et al. 2008). In addition, cold pools associated with precipitation downdrafts impact the boundary layer (Feng et al. 2015; de Szoeke et al. 2017). Cold pools occurred during DYNAMO in association with isolated convection, organized convective systems, and the ITCZ, the last being a prominent feature $\sim 5^{\circ}$ south of the equator during the early October suppressed period (Moteki 2015; Ciesielski et al. 2018).

The purpose of this paper is to investigate the evolution of the atmospheric boundary layer during the onset of the DYNAMO October MJO and to document the subcloud atmospheric mixed layer at the *R/V Revele* during the early period of convective development. A simple heat budget is used as a diagnostic for the mixed layer depth taking into account horizontal advective effects arising from SST gradients and/or convective cold pools, observations of the surface buoyancy flux, and estimates of the mixed layer net radiative heating rate. The results of this paper have implications for simulating the MJO in models that include parameterized cloud and turbulence scale motions. They are also relevant to climate system modeling in general, which is critically dependent upon coupling between the atmosphere and ocean.

2. Quasi-equilibrium mixed layer heat budget

During the suppressed periods, cumulus clouds are widely scattered and to a first approximation, we neglect cloud effects and assume that radiative heating is the only mixed layer (ML) diabatic process. The Reynolds-averaged expression for the virtual potential temperature $\theta_v = \theta(1 + 0.61q)$ is then

$$\frac{\partial \bar{\theta}_v}{\partial t} + \bar{\mathbf{v}} \cdot \nabla \bar{\theta}_v + \bar{w} \frac{\partial \bar{\theta}_v}{\partial z} = -\frac{\partial \overline{w'\theta'_v}}{\partial z} + Q_R, \quad (1)$$

where Q_R is the radiative heating rate; overbars indicate a time average and primes a deviation from that average. The time rate of change of daily-averaged values of $\bar{\theta}_v$ is $\sim 0.1^{\circ}\text{C day}^{-1}$ while Q_R is $\sim 1\text{--}2^{\circ}\text{C day}^{-1}$, so we neglect the local change term in (1).¹ However, horizontal advection cannot be neglected due to flow across strong SST gradients and temperature fluctuations due to nearby convection. Integration of (1) from the ocean surface to the top of the ML z_i assuming constant $\bar{\mathbf{v}}$, $\bar{\theta}_v$, and Q_R in the ML yields

$$\bar{\mathbf{v}} \cdot \nabla \bar{\theta}_v = \frac{F_s - F_i}{\bar{\rho} c_p z_i} + Q_{Rm}, \quad (2)$$

where F_s and F_i are the buoyancy fluxes [$\approx \bar{\rho} c_p (\overline{w'\theta'} + 0.61 \overline{w'q'})$; in W m^{-2}] at the surface and z_i , respectively; $\bar{\mathbf{v}}$, $\bar{\theta}_v$, and Q_{Rm} are ML-mean values; and ρ is air density. Equation (2) is a statement that under steady-state and cloud-free conditions the eddy flux convergence of heat in the ML is balanced by the combined effects of advection and radiative

¹ This approximation will be shown to be valid with reference to later Fig. 8.

cooling of that layer. The value of z_i in (2) can be considered an equilibrium ML depth for a quasi-steady and cloud-free boundary layer, referred to here as z_{ieq} .² Using the closure $F_i = -kF_s$ for free convection,

$$\bar{v} \cdot \nabla \bar{\theta}_v = \frac{(1+k)F_s}{\bar{\rho} c_p z_{ieq}} + Q_{Rm}, \quad (3)$$

where k is a positive constant, here taken to be 0.2 (Deardorff et al. 1969).

From (3),

$$z_{ieq} = \frac{(1+k)F_s}{\bar{\rho} c_p (\bar{v} \cdot \nabla \bar{\theta}_v - Q_{Rm})}. \quad (4)$$

The diagnostic relationship (4) represents an alternative to predicting z_i , thereby eliminating the need for an entrainment parameterization. The convective boundary layer heat budget evolves toward this equilibrium state, for example, during the ML recovery following a cool precipitation downdraft wake. The equilibrium should be attained on the entrainment time scale $T_{ent} \sim (\Delta\theta_v)^2 / (\Gamma_{\theta_v} k F_s) \approx 6$ h (derived in the appendix). The ML equilibrium heat budget z_{ieq} also defines a subcloud equilibrium heat content.

We exploit the concept of the equilibrium mixed layer and whether it is coupled to the cloud layer. Clouds will develop when the mixed layer depth reaches the lifting condensation level (LCL) of the mixed layer air. Under this scenario, if $z_i < \text{LCL}$, the mixed layer warms and entrains and $dz_i/dt > 0$ until $z_i = z_{ieq}$ and $d\theta_v/dt = dz_i/dt = 0$, where z_{ieq} is given by Eq. (4). If $z_{ieq} \geq z_i \geq \text{LCL}$, assumptions leading to Eq. (4) are no longer valid and the mixed layer conditions already favor moist convection.

Changes to advection and radiation have implications on z_{ieq} through (4), which may act to strengthen the development of the MJO. Advection of warm, moist air ($\bar{v} \cdot \nabla \bar{\theta}_v < 0$) also has the effect of reducing the denominator in (4), resulting in a deeper mixed layer. Since $Q_{Rm} < 0$, a reduction in the radiative cooling rate yields a deeper mixed layer, everything else being the same. This situation could occur, for example, if cirrus clouds were to advance into the region late in the suppressed period, which is supported by observations during DYNAMO (Johnson et al. 2015) and found to be a characteristic feature of MJOs in composite studies (Virts and Wallace 2010; Del Genio et al. 2012).

3. Data and methods

The behavior of the mixed layer during the October MJO initiation is based on observations from the *R/V Revelle*. *Revelle* is the most appropriate DYNAMO site for this analysis since it best represents open-ocean conditions along the

equator. The other near-equatorial site is Gan Island (Addu Atoll), which is significantly influenced by land/atoll effects (Johnson and Ciesielski 2017; Ciesielski and Johnson 2021).

a. Sounding observations

Radiosonde data from five stations in the DYNAMO sounding arrays are used to document the boundary layer structure and determine the mixed layer (ML) depth when well-mixed profiles in potential temperature and specific humidity existed (Johnson and Ciesielski 2017). Soundings are identified as having MLs if both of the following conditions are met: θ is approximately constant with height from the surface (or the top of a superadiabatic layers when it exists) up to a height z_i , the ML top, with an abrupt increase in stability above z_i ; and q is constant or decreases only slightly from the surface up to z_i and then decreases rapidly above. A comparison of ML depths determined by this procedure with those based on turbulent kinetic energy dissipation rates (next subsection) is presented in section 4b.

b. Turbulent kinetic energy dissipation rate

The depth of the atmospheric boundary layer is also determined from turbulent kinetic energy dissipation rate (ϵ) data from the NOAA High-Resolution Doppler lidar aboard the *Revelle*. These data have been used by de Szoeke et al. (2020) to investigate the diurnal variation of the ML during the November suppressed period. We employ their procedure to determine the ML depth as the lowest height at which ϵ is less than the mean below that height by a factor of 3.

c. Radiative heating rates

Direct measurements of the radiative heating rates in the boundary layer at the *Revelle* are not available, so we have used a procedure that translates the Combined Retrieval (CombRet) radiative heating rates from Gan Island (Feng et al. 2014) to the *Revelle* location with appropriate modifications that involve the use of the Clouds and Earth's Radiant Energy System (CERES) V4.1 product at 3-hourly intervals on a 1° grid (Wielicki et al. 1996). The CombRet data are available at 5-hPa vertical resolution while the CERES data are available at only six levels, two of which are the surface and 850 hPa. Average radiative heating rates Q_R for the surface to 850-hPa layer at Gan are computed using radiative fluxes from CERES and then compared to CombRet values for that layer. The plan was to use this comparison of Q_R for the October suppressed period at Gan and then, assuming the CombRet values are more accurate, adjust CERES-based Q_R estimates at the *Revelle* by the average bias for that period. Since our study involves the boundary layer, whose depth is closer to the surface-950 hPa layer than the surface-850 hPa layer, there is an additional adjustment of the biases to the shallower layer based on a comparison of average CombRet Q_R for the two layers. Since the CombRet product is not available prior to 10 October, we instead use the bias estimate for the November suppressed period (4–15 November) assuming the all-sky conditions then most closely equate to those during the October suppressed period. The net effect is

² A related argument has been made for the momentum balance of a steady boundary layer (Samelson et al. 2006), where a quasi-equilibrium analytical model shows the surface stress (as opposed to the surface buoyancy flux in our case) to be directly proportional to the boundary layer depth z_i .

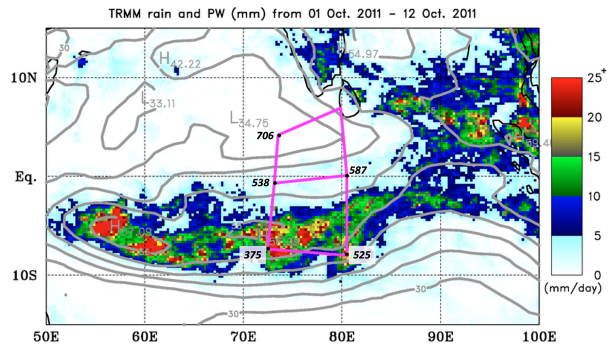


FIG. 2. 1–12 Oct mean TRMM rainfall (mm day^{-1}) and precipitable water (PW; contours; 5 mm intervals) over Indian Ocean DYNAMO array. Values at vertices of sounding array quadrilaterals indicate 1–12 Oct mean mixed layer depths (m) for the approximately two-thirds of the time that well-mixed boundary layers were observed.

to add a small amount of cooling (0.21 K day^{-1}) to the CERES flux-based estimates of Q_R for the surface to 950-hPa layer. This adjustment agrees with the conclusions of Shell et al. (2020).

d. Gridded satellite and analysis products

Large-scale fields over the Indian Ocean and computations of ML depth at the *Revelle* from (4) are based on the European Centre for Medium-Range Weather Forecasts (ECMWF) Operational Analysis (OA) product at 0.25° horizontal resolution, with 18 vertical levels from the surface to 50 hPa, and at 6-hourly intervals (Johnson and Ciesielski 2013). The ECMWF OA dataset incorporates the majority of the soundings from the DYNAMO arrays and is found to be in good agreement with the CSU gridded dataset based on quality-controlled soundings (Johnson and Ciesielski 2013; Ciesielski et al. 2014). The choice of the ECMWF OA product over the CSU gridded analyses to compute the heat budget at the *Revelle* is based on its ability to better resolve localized gradients and hence provide superior estimates of advective effects. Observed sounding ML profiles are compared to two reanalysis products: the ECMWF OA and the ERA5 Global Reanalysis (Hersbach et al. 2020), both at 0.25° horizontal resolution. Rainfall data are from the Tropical Rainfall Measuring Mission (TRMM) 3B42v7 3-hourly, $0.25^\circ \times 0.25^\circ$ product (Huffman et al. 2007), and rainfall and radar reflectivity data are from the TOGA radar aboard the *Revelle* (Xu and Rutledge 2014). The climatology of the surface winds over the Indian Ocean is based on the National Aeronautics and Space Administration Quick Scatterometer (QuikSCAT), which provides twice per day wind estimates at 25-km horizontal resolution. Basinwide sea surface temperature (SST) data are from the Woods Hole Oceanographic Institution (WHOI) OAFlex product (Yu and Weller 2007) available daily at 1° horizontal resolution. The CERES product is also used to obtain fractional cloudiness data. Surface fluxes and SST data at the *Revelle* are from in situ measurements aboard the ship (de Szoeke et al. 2015).

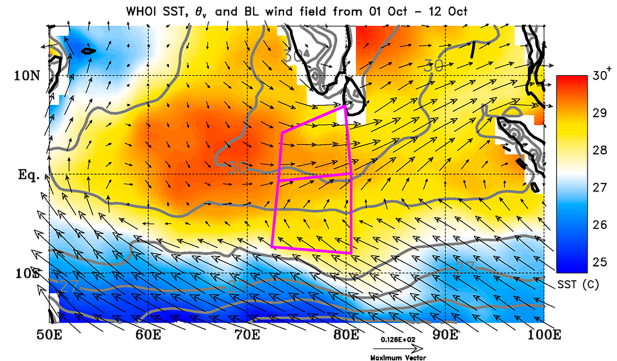


FIG. 3. 1–12 Oct mean SST (color; $^\circ\text{C}$), boundary layer (surface-to-950-hPa mean) wind (m s^{-1}), and boundary layer virtual potential temperature θ_v (contours; 1°C intervals) over the Indian Ocean. Polygons denote DYNAMO sounding arrays.

4. Results

a. Initiation of October MJO

Figure 2 shows the 1–12 October mean TRMM rainfall, precipitable water, and mixed layer (ML) depths at five sounding sites over the Indian Ocean. This time period corresponds to the developing phase of the October MJO when the southern ITCZ was active and dry air was present over the northern sounding array (Ciesielski et al. 2018). Correspondingly, the mean ML depths at Diego Garcia and the research vessel *Mirai* were relatively low as a result of numerous incidences of precipitation downdraft wake recovery, while deep MLs were observed at Malé in association with dry conditions there. ML depths at Gan and the *Revelle* were close to their DYNAMO means. The study by Moteki (2015) showed that the initiation of the MJO was associated with a shift in the southern Indian Ocean ITCZ in Fig. 2 toward the equator by the middle of October.

The mean boundary layer (surface to 950 hPa) wind and θ_v fields and sea surface temperature (SST) for 1–12 October are shown in Fig. 3. A warm SST anomaly was centered in a region of cross-equatorial, converging surface airflow just north of the equator between 60° and 70°E . Air entering this region from both sides of the equator passed from cooler to warmer water, enhancing surface buoyancy fluxes. This flow configuration also promotes mixed layer growth, assuming lower-tropospheric subsidence does not change significantly. While surface fluxes directly impact boundary layer properties, the mean boundary layer θ_v field does not conform exactly to the SST distribution. In particular, a departure from the SST field exists around the Indian subcontinent where that heated landmass has apparently warmed the surrounding atmosphere.

Beginning around 15 October, precipitation started developing over the equatorial region within 55° – 75°E (Fig. 4). This longitude span marks the location of the initiation of the October MJO (Gottschalck et al. 2013; Yoneyama et al. 2013; Johnson and Ciesielski 2013). Broadly speaking, this region coincides with an area where the surface flow was converging into the equatorial SST maximum (Fig. 3). Prior studies have argued that this surface convergence is largely driven by SST

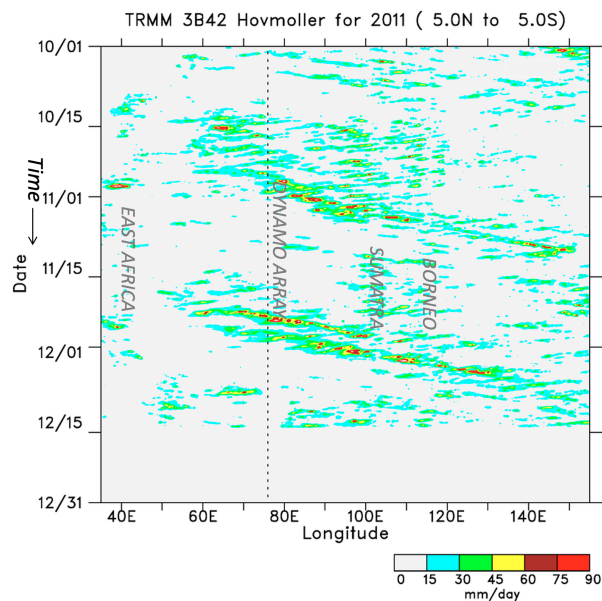


FIG. 4. Time-longitude plot of TRMM 3B42 precipitation (mm day^{-1}) from 35° to 155°E averaged from 5°N to 5°S for the period 1 Oct–31 Dec 2011. Vertical dashed line denotes the center of the DYNAMO sounding arrays.

gradients in the region (Carbone and Li 2015; Rydbeck et al. 2017; de Szoeke and Maloney 2020).

b. Mixed layer evolution at Revelle

A time series of sounding-based atmospheric ML depths at the *Revelle* is shown in Fig. 5a. ML depths increased during the suppressed, light-rain period from 1 to 12 October, then decreased rapidly as rain began to ramp up in the middle of the month (Fig. 5c). The shallower MLs are a reflection of recovering mixed layers following precipitation downdrafts (de Szoeke et al. 2017). The October suppressed period was marked by gradually increasing SST having a $\sim 0.5^{\circ}\text{C}$ amplitude diurnal cycle (Fig. 5b). There was another suppressed period leading up to the second MJO in early November; however, the *Revelle* was off station during that period. There was also an ~ 5 -day period with little-to-no rainfall in mid-November characterized by relatively deep mixed layers and a large-amplitude diurnal SST cycle (Ruppert and Johnson 2015; Johnson and Ciesielski 2017; de Szoeke et al. 2020). However, given the shortness of this latter suppressed period and the data gap for the early-November period, we focus in this study on the October suppressed period. While there was minimal rainfall during this period, there were moderately strong surface winds ($\sim 5 \text{ m s}^{-1}$). Nevertheless, there was an SST diurnal cycle and the development of a diurnal warm layer in the upper ocean (Moulin et al. 2018). The average ratio of the ML depth to the negative of the Monin–Obukhov length ($-c_p \bar{\rho} \theta_{vs} u_s^3 / kg F_s$, where u_s is the friction velocity and k is the von Kármán constant) during this period was ~ 10 , indicating the dominance of buoyancy over shear in producing

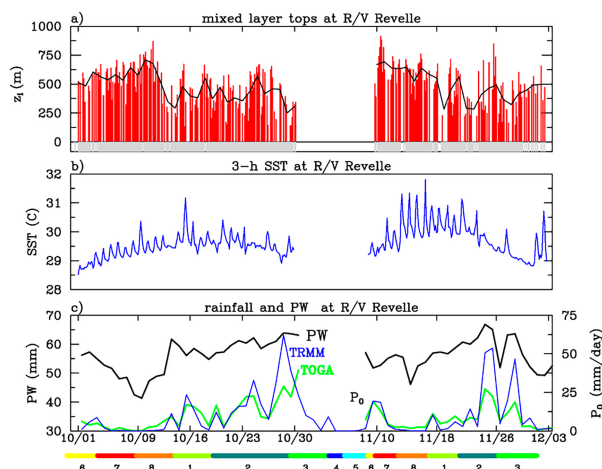


FIG. 5. Time series from 1 Oct to 3 Dec at *Revelle* of (a) sounding-based atmospheric mixed layer depths at 3-h intervals (red bars; m), with solid line indicating daily-average values; (b) 3-hourly *Revelle* SST ($^{\circ}\text{C}$) at 0.1 m depth; and (c) precipitable water (mm) and precipitation rate (mm day^{-1}) from TRMM and the TOGA radar. Gray bars at bottom of (a) indicate times at which soundings were taken. Color bars at bottom of figure indicate phases of Wheeler and Hendon's (2004) RMM index.

turbulent kinetic energy (TKE) throughout most of the depth of the ML.

TKE dissipation rate ϵ at the *Revelle* for the early October suppressed period is shown in Fig. 6a. Consistent with sounding-based ML data (Fig. 5a), the turbulence data indicate a gradually deepening boundary layer up until 11 October followed by a reduction of depths with the onset of rainfall. Comparison of daily-averaged ML depths determined from

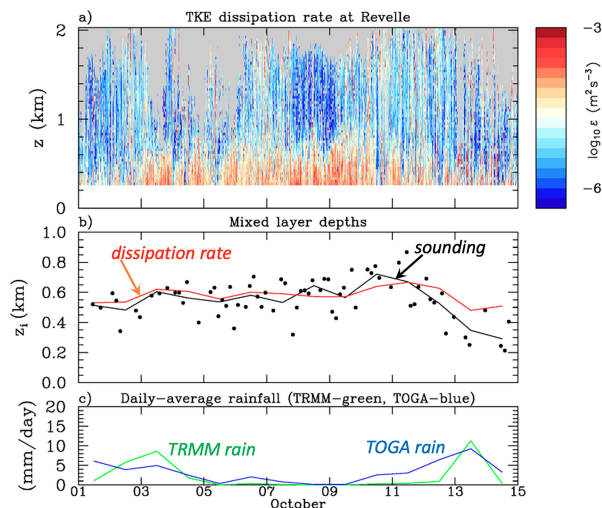


FIG. 6. (a) TKE dissipation rate ϵ ($\log_{10}\epsilon; \text{m}^2 \text{s}^{-3}$), (b) ML depths determined from sounding data (black dots) and comparison of daily-average ML depths from soundings (black curve) and TKE dissipation rates (red curve), and (c) daily-average rainfall from the TOGA radar (blue) and from TRMM averaged over the TOGA radar domain for 1–15 Oct.

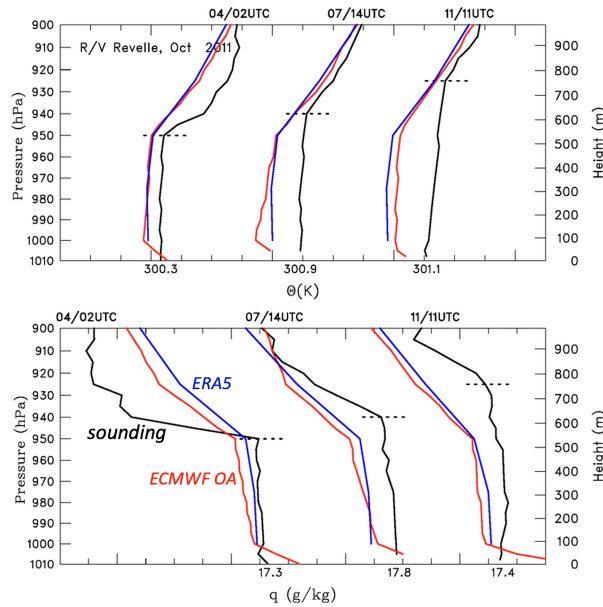


FIG. 7. Vertical profiles of (top) potential temperature (K) and (bottom) specific humidity (g kg^{-1}) on 4, 7, and 11 Oct from soundings (black), ECMWF OA (red), and ERA5 (blue). Tick mark intervals are 1 K at top and 1 g kg^{-1} at bottom. Times after dates at top are in UTC. Dotted lines denote estimates of ML top.

soundings and TKE dissipation rate data (Fig. 6b) shows that the two agree well up until the onset of rainfall (correlation coefficient = 0.83).

ML potential temperature and specific humidity profiles during the first part of October are shown in Fig. 7. The three dates were selected to represent the ML profile evolution during the lightest rainfall period (Fig. 6c). The *Revelle* soundings (black) show a deepening ML over this 1-week period, accompanied by a slight surface warming and progressively less distinct well-mixed profiles. The ML structures represented by ECMWF OA and ERA5 agree reasonably well with the observations on 4 October, but later diverge as the observed soundings warm while the ECMWF profiles do not. The departures are significant even considering the coarse vertical resolution of ECMWF data, indicating shortcomings in the analysis products in capturing the evolving boundary layer during the October MJO initiation. In addition to differences in the vertical structures, rather substantial boundary layer cool and dry biases are apparent in the ECMWF data, as pointed out by Ciesielski et al. (2021).

An expanded view of the early October suppressed period is shown in Fig. 8. The first four days of October were characterized by light rain and some high clouds, followed by a mostly dry period until about 9/10 October, then concluding with increased rainfall and high clouds (Fig. 8a). Cloud development during this suppressed period transitioned from shallow cells organized in shear-parallel lines to progressively deeper convection organized along cold pool boundaries (Rowe and Houze 2015). Until about 12 October, the surface buoyancy flux was roughly constant (Fig. 8b). Throughout the period, the

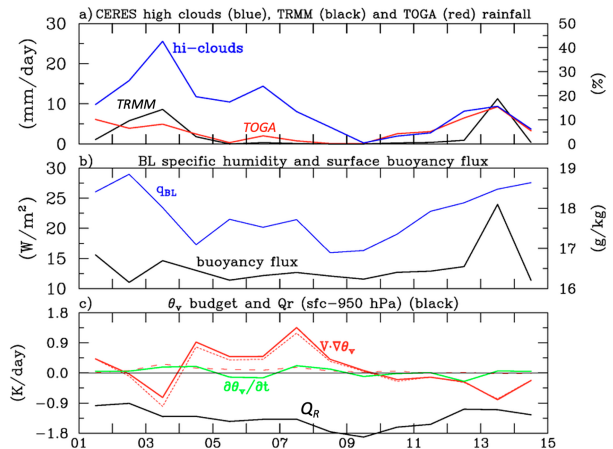


FIG. 8. Time series from 1 to 15 Oct at *Revelle* of daily-averaged (a) CERES high cloud fraction (%) and TRMM and TOGA rainfall rate (mm day^{-1}); (b) surface buoyancy flux (W m^{-2}) and boundary layer specific humidity q_{BL} (g kg^{-1}); and (c) local and horizontal advective changes in θ_v . In (c) dotted and dashed red curves represent θ and q contributions to θ_v advection, respectively; surface to 950-hPa radiative heating rate Q_R .

local change in θ_v was small compared to horizontal advection and radiative cooling (Fig. 8c). During the most suppressed conditions (4–9 October), lower θ_v was being advected into the region, then higher θ_v was advected in after 9 October (Fig. 8c).

Computations of ML depth from (4) using $k = 0.2$ are carried out for the 4–11 October light-rain period (TOGA rain rate $< 5 \text{ mm day}^{-1}$) with and without effects of advection included. Inclusion of advective effects brings the diagnosed ML depth into better agreement with the observed evolution over the course of this dry period (Fig. 9a). The increase in the ML depth after the 9th corresponded to the start of reduced radiative cooling rates (Fig. 8c), which from the balance condition (4) would lead to an increased z_i .

The interpretation of these results is as follows. The concurrent increase in ML depth and reduction in the LCL during the 9–11 October period resulted in a greater number of boundary layer eddies reaching the condensation level and forming cumulus clouds. Figure 9b depicts the evolution of the SPOL radar echo area and 0-dBZ echo-top heights. Intermittent deep convection occurred during the first 4–5 days of October, followed by scattered, mostly shallow convection over the next week, then a resurgence of deep convection after the 11th. At the start of this latter period, gradual lowering of the LCL commenced as a result of increasing moistening (Fig. 8b), such that mixed layers depths began to rise above the LCL (Fig. 9a), resulting in an enhancement of convective activity. The increase in deep convection was also aided by a substantial increase in column moisture starting on 9 October (Fig. 5c) that took place in the lowest 5 km over the following 4–5 days (Johnson and Ciesielski 2013; de Szoeke et al. 2015; Powell and Houze 2015b). Moreover, the early October period was accompanied by steadily increasing SSTs, leading to increased CAPE (Xu and Rutledge 2014), as well as a modest

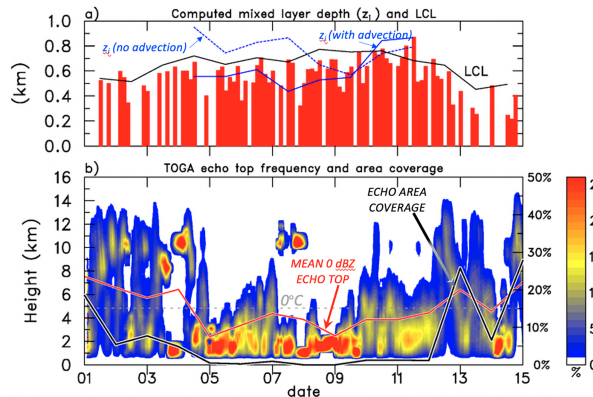


FIG. 9. Time series from 1 to 15 Oct at *Reville* (a) mixed layer depths from soundings (red bars; m), computed daily-average mixed layer depth z_i including horizontal advection (solid blue) and excluding horizontal advection (dashed blue), daily-average lifting condensation level LCL based on mixed layer mean conditions (black) and (b) TOGA radar-echo area coverage (black curve; %; scale on right axis) and 0-dBZ echo-top height frequency (color; %; mean value shown by red curve). The echo-top frequency is computed such that at each time (10-min resolution) the total percentage of all vertical levels is equal to one. Gray dashed line denotes 0°C level.

SST diurnal cycle, which can act to accelerate the onset of deep convection (Ruppert 2016).

The computations from (4) shown in Fig. 8a of the mixed layer depth during the early October suppressed period show that the boundary layer properties were significantly influenced by advective effects. From 4 to 9 October, cool (low θ_v)-air advection was present at the *Reville*, followed by weak warm air advection (Fig. 8c). The flow configuration during the period of peak cool-air advection is shown in Fig. 10a. During this time, cool air was advected into the *Reville* area from the ITCZ region in the Southern Hemisphere, which required a shallower ML depth than would otherwise be diagnosed without advection (Fig. 8a).

Following this period, from 9 to 12 October, the advective term decreased to near zero (Fig. 8c). Winds in proximity to the *Reville* shifted to more westerly (Fig. 10b) leading to weaker θ_v advection. Therefore, the increase in the diagnosed ML depths from 9 to 12 October (Fig. 9a) are primarily attributable to the decrease in radiative cooling rate (Fig. 8c). This reduction in radiative cooling was accompanied by an increase in high clouds (i.e., cirrus; Fig. 8a). Assuming the reduced radiative cooling was caused by the clouds, we have a remarkable situation where the z_{req} of the boundary layer is modified by increasing high clouds vertically far removed from it. Also assuming the radiative cooling in the ML is comparable to that just above it in the free troposphere and making the weak temperature gradient approximation that this cooling is balanced by subsidence warming, the reduced ML cooling rate late in the period under study is also consistent with reduced subsidence found to occur during the MJO onset phase (Powell and Houze 2015a). However, sorting out the relationship between Kelvin wave anomalous lifting, cirrus, and ML evolution is beyond the scope of this study.

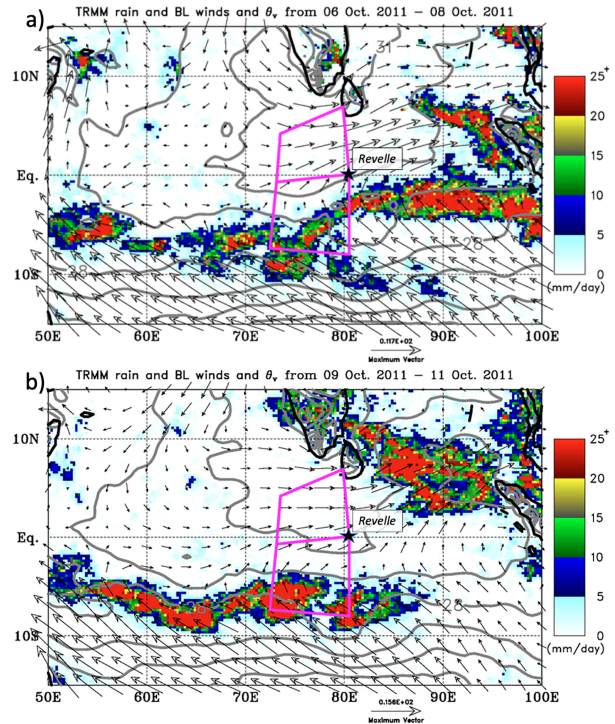


FIG. 10. Surface to 950-hPa mean θ_v ($^\circ\text{C}$), surface wind (m s^{-1}), and TRMM rainfall (mm day^{-1}) over the Indian Ocean for (a) 6–8 Oct and (b) 9–11 Oct.

5. Parsing the contributions to boundary layer horizontal advection

The boundary layer advection of θ_v at the *Reville* can be attributed to 1) flow across gradients in SST, to the extent those gradients are communicated to the boundary layer air, and/or 2) low-level θ_v gradients due to convective activity and associated cold pools. Moteki (2015) investigated the relationship between gradients in both SST and surface potential temperature for the 9–14 October period and found that the meridional gradients of these quantities mirrored each other over the DYNAMO domain between the equator and $\sim 5^\circ\text{S}$. His findings suggest that the advection of θ_v at low levels in the boundary layer is principally related to SST gradients. To estimate the portion of the boundary layer θ_v advection due to flow across SST gradients, we compute $\mathbf{v} \cdot \nabla \text{SST}$, referred to here as SST advection, where \mathbf{v} is the boundary layer-averaged wind.

However, closer examination of Fig. 10 suggests another factor may be at play. The figure indicates that the ITCZ was relatively close to the *Reville* during 6–8 October (Fig. 10a) compared to its 1–12 October mean position (Fig. 2) or its position on 9–11 October (Fig. 10b). Cold advection increased during 6–8 October (Fig. 8c), suggesting that the cooler air was likely associated with precipitation downdrafts from the nearby ITCZ band. A comparison of advections from boundary layer θ_v and SST is shown in Fig. 11. Cool advection exists in both fields over much of the Indian Ocean south of the equator due to flow from cooler to warmer waters (Fig. 3).

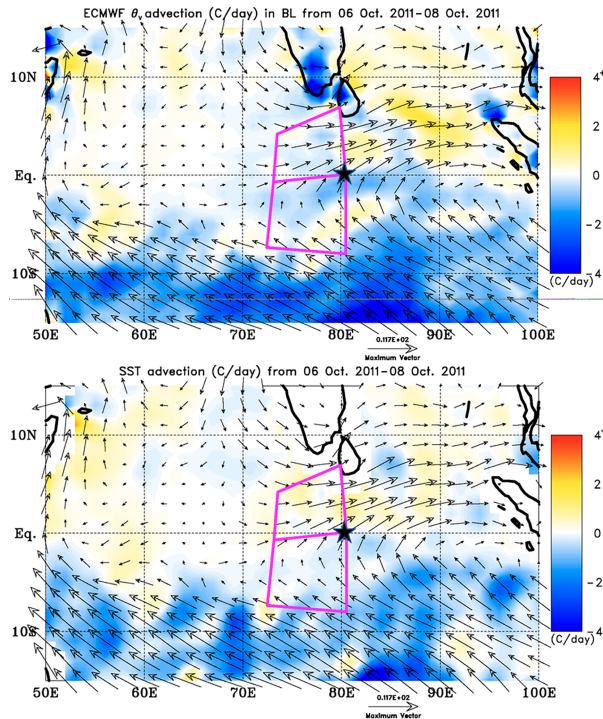


FIG. 11. 6–8 Oct mean surface wind (m s^{-1}) and advection ($^{\circ}\text{C day}^{-1}$) associated with (a) surface-950-hPa θ_v (i.e., $-\mathbf{v} \cdot \nabla \theta_v$) and (b) SST (i.e., $-\mathbf{v} \cdot \nabla \text{SST}$). Black star denotes position of *Revelle*.

However, just south of the *Revelle*, θ_v cool advection exceeds that associated with SST, indicating that cool low-level outflow from the ITCZ band is the dominant advective process during this period. A comparison of θ_v and SST advection for the entire 1–12 October period (Fig. 12a) shows that the boundary layer advection at the *Revelle* is largely independent of SST gradients, indicating that transient convective activity is the primary driver of advective effects there. A similar behavior is seen farther south at the *Mirai* (Fig. 12b) where there was considerable short-term variability in θ_v advection. However, at this location there was persistent cold advection due to flow across the strong SST gradients south of the *Mirai* (Fig. 3).

6. Summary and conclusions

This study has investigated the evolution of the atmospheric mixed layer at the *Revelle* during the lead-up to increased convective activity over the Indian Ocean associated with the October 2011 MJO. The first third of October was a period of generally suppressed convection with cloud development increasing toward the end of this period. The mixed layer depth grew from ~ 500 to ~ 700 m from 1 to 11 October. A heat budget that defines an equilibrium mixed layer is developed and applied to the quasi-steady, mostly clear conditions that existed during the most suppressed portion of this early October period. Application of the diagnostic relationship that is developed shows that horizontal advection was an

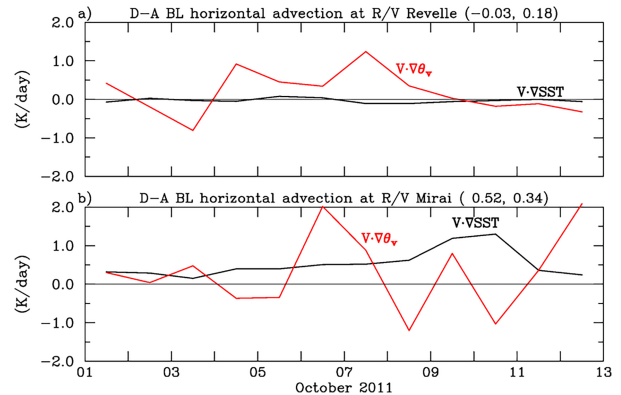


FIG. 12. The 1–12 Oct daily-averaged (D-A) advection associated with boundary layer θ_v (red) and SST (black; $^{\circ}\text{C day}^{-1}$) at the (a) *Revelle* and (b) *Mirai*. Advection is computed within 1° radius of each ship. Numbers in parentheses represent the period means for the SST and θ_v advection, respectively.

important factor in explaining the mixed layer evolution at the *Revelle* from 4 to 9 October. While cold advection due to SST gradients was a dominant feature over much of the Indian Ocean south of the equator, low-level cold outflow from a band of ITCZ convection between 0° and 5°S was the primary contributor to cold advection at the *Revelle* during this period. The following 9–12 October period saw much reduced horizontal advective effects, so the increase in the equilibrium ML depth during that time was related to decreased radiative cooling in the boundary layer. This reduction in radiative cooling coincided with increasing cirrus clouds in advance of the active phase of the MJO. This finding reveals a rather unique influence cirrus had during this period; namely, its radiative impact led to an increase in the equilibrium ML depth far from it. Toward the end of the suppressed period, the deepening mixed layer eventually reached the lifting condensation level of the boundary layer, resulting in an increasing number of cumulus clouds prior to the active phase of the October MJO.

The mixed layer depth is a valve for initiating shallow convection as it approaches the lifting condensation level, and air entering the bases of cumulus clouds comes from the subcloud mixed layer. Accurate representation of the boundary layer in global models is thus needed to properly handle cloud evolution and MJO convective initiation, especially as model resolution continues toward explicit treatment of convection. More broadly, realistic simulations of the global tropical climate depend upon accurate treatment of boundary layer processes. The results here indicate that the inversion height is attracted to an equilibrium inversion height that balances the heat budget. This equilibrium inversion height varies on intraseasonal rather than hourly time scales. Models should be able to reproduce this inversion height, and how fast it reestablishes itself if conditions such as surface flux or advection change. The nearly constant ML depths seen in the ECMWF OA and ERA5 during the October early-onset period as opposed to the observed ML depth increase (Fig. 7) indicate

that mixed layer properties remain a modeling problem. The results suggest the use of the expression for equilibrium mixed layer depth z_{ieq} as a metric for readily evaluating large-scale mixed layer evolution in models, and the sensitivity of their convection to the mixed layer.

Acknowledgments. Richard Johnson and Paul Ciesielski acknowledge support from the National Science Foundation under Grant AGS-1853633 and Simon de Szoeké acknowledge support from the National Oceanic and Atmospheric Administration Climate Variability and Predictability Grant NA19OAR4310375 and Office of Naval Research Grant N00014-22-1-2042. Brian McNoldy is acknowledged for his assistance with Fig. 1. We thank three anonymous reviewers for very helpful comments and suggestions.

Data availability statement. The CERES cloud and microphysical data were obtained from <http://ceres.larc.nasa.gov/products.php?product=SYN1deg>, the CombRet cloud microphysical data from <https://www.arm.gov/data/pi/71>, the SPOL legacy radar data from <https://data.eol.ucar.edu/project/DLDP>, the TRMM rainfall data from https://disc.gsfc.nasa.gov/datasets/TRMM_3B42_7/summary, the OAF flux surface fluxes from <https://researchdata.edu.au/woods-hole-oceanographic-v3-daily/15322>, the CSU gridded diagnosed fields from <https://data.eol.ucar.edu/dataset/347.240>, the ERA5 data from <https://www.ecmwf.int/en/forecasts/datasets/reanalysis-datasets/era5>, the TKE dissipation rate data from NOAA Chemical Sciences Division: <https://csl.noaa.gov/groups/csl3/measurements/2011dynamo/calendar.php>, and the QuikSCAT data from <https://podaac.jpl.nasa.gov/QuikSCAT>.

APPENDIX

Equilibrium Time Scale

Without considering time dependence, we defined the equilibrium inversion height z_{ieq} that balances the heat budget. This is like assuming that the inversion z_i adjusts very fast to changes in the heat budget. If the mixed layer is shallow, then the turbulence flux divergence $(1+k)F_s/(\bar{\rho}c_p z_i)$ warms it up quickly. Yet z_i also deepens in this process, as entrainment outpaces mean subsidence, until z_i reaches z_{ieq} . Any change in the turbulent heat flux $(1+k)F_s$, radiative heat source Q_R , or advective heat source $\mathbf{v} \cdot \nabla \theta_v$, results in a transient imbalance that is restored by entrainment. The equilibrium inversion height is obtained on the time scales of interest if z_i adjusts much faster by entrainment than intraseasonal changes in the heat budget.

How quickly does z_i adjust? In this appendix, we show that entrainment across a discontinuous zero-order jump of virtual potential temperature $\Delta\theta_v$ overlain by moist adiabatic stratification tends toward an inversion height on a time scale of about 6 h, much faster than the variations of z_{ieq} that are shown to be correlated to daily-to-intraseasonal convective variability.

The equation for virtual (density) potential temperature flux continuity across an inversion at height z_i (e.g., Lilly 1968) is

$$(\partial z_i / \partial t - w) \Delta \theta_v + F_{i-} = R_+, \quad (\text{A1})$$

where $\Delta\theta_v = \theta_{v+} - \bar{\theta}_v$ is the virtual potential temperature jump, above (θ_{v+}) minus below $(\bar{\theta}_v)$ the inversion, and w is the mean vertical velocity. Equation (A1) states that the decrease in temperature due to entrainment and the upward turbulent heat flux from below the inversion F_{i-} are balanced by the upward radiative heat flux R_+ . The radiative flux below the inversion R_- and the turbulent flux above the inversion F_{i+} are assumed to be zero. Assuming clouds are not found below the inversion, the net flux above the inversion R_+ will also be neglected henceforth. The turbulent virtual potential temperature flux below the inversion is proportional to the surface flux as above, $F_{i-} = -kF_s$, with $k = 0.2$.

The equation for the inversion height z_i becomes

$$\partial z_i / \partial t = w + kF_s / \Delta \theta_v. \quad (\text{A2})$$

The jump $\Delta\theta_v$ evolves with the lapse rate of virtual potential temperature above the inversion Γ as

$$\frac{\partial(\Delta\theta_v)}{\partial z_i} = \frac{\partial\theta_v}{\partial z} = \Gamma. \quad (\text{A3})$$

Then linearizing $(\Delta\theta_v)^{-1} \approx (\Delta\theta_v)_{ent}^{-1} + (\Delta\theta_v)_{ent}^{-2} \Gamma (z_i - z_{ient})$ as a perturbation $z'_i = z_i - z_{ient}$ about an equilibrium inversion height z_{ient} with inversion strength $(\Delta\theta_v)_{ent}$, the z_i equation becomes

$$\frac{\partial z_i}{\partial t} = w + \frac{kF_s}{(\Delta\theta_v)_{ent}} - \frac{kF_s}{(\Delta\theta_v)_{ent}^2} \Gamma (z_i - z_{ient}).$$

Note for $\partial z_i / \partial t \rightarrow 0$, $z_i \rightarrow z_{ient}$ and $(\Delta\theta_v)_{ent} = -kF_s/w$. Dropping the subscript from $(\Delta\theta_v)_{ent}$, the time-dependent equation is

$$\frac{\partial z'_i}{\partial t} = -\frac{kF_s \Gamma}{(\Delta\theta_v)^2} z'_i$$

and the inversion height z_i approaches z_{ient} with a time scale

$$\tau_i = \frac{(\Delta\theta_v)^2}{\Gamma k F_s}. \quad (\text{A4})$$

To make things concrete, we take reasonable values $\Gamma = 3 \times 10^{-3} \text{ K m}^{-1}$ for a moist adiabat, $\Delta\theta_v = 0.5 \text{ K}$, $k = 0.2$, and $(w'\theta'_v)_0 = 2 \times 10^{-2} \text{ K ms}^{-1}$, corresponding to a sensible heat flux of 10 W m^{-2} and the density effect of a latent heat flux of 200 W m^{-2} . For these values the time scale for the inversion height adjustment is $\tau_i = 5.6 \text{ h}$.

REFERENCES

- Bellenger, H., Y. N. Takayabu, T. Ushiyama, and K. Yoneyama, 2010: Role of diurnal warm layers in the diurnal cycle of convection over the tropical Indian Ocean during MISO. *Mon. Wea. Rev.*, **138**, 2426–2433, <https://doi.org/10.1175/2010MWR3249.1>.
- Bernie, D. J., E. Guilyardi, G. Madec, J. M. Slingo, S. J. Woolnough, and J. Cole, 2008: Impact of resolving the diurnal cycle in an ocean–atmosphere GCM. Part 2: A diurnally coupled CGCM.

- Climate Dyn.*, **31**, 909–925, <https://doi.org/10.1007/s00382-008-0429-z>.
- Carbone, R. E., and Y. Li, 2015: Tropical oceanic rainfall and sea surface temperature structure: Parsing causation from correlation in the MJO. *J. Atmos. Sci.*, **72**, 2703–2718, <https://doi.org/10.1175/JAS-D-14-0226.1>.
- Chen, X., and F. Zhang, 2019: Relative roles of preconditioning moistening and global circumnavigating mode on the MJO convective initiation during DYNAMO. *Geophys. Res. Lett.*, **46**, 1079–1087, <https://doi.org/10.1029/2018GL080987>.
- Ciesielski, P. E., and R. H. Johnson, 2021: Small island effects in DYNAMO and their impact on large-scale budget analyses. *J. Appl. Meteor. Climatol.*, **60**, 577–594, <https://doi.org/10.1175/JAMC-D-20-0238.1>.
- , and Coauthors, 2014: Quality controlled upper-air sounding dataset for DYNAMO/CINDY/AMIE: Development and corrections. *J. Atmos. Oceanic Technol.*, **31**, 741–764, <https://doi.org/10.1175/JTECH-D-13-00165.1>.
- , R. H. Johnson, W. H. Schubert, and J. H. Ruppert Jr., 2018: Diurnal cycle of the ITCZ in DYNAMO. *J. Climate*, **31**, 4543–4562, <https://doi.org/10.1175/JCLI-D-17-0670.1>.
- , —, S. Tang, Y. Zhang, and S. Xie, 2021: Comparison of conventional and constrained variational methods for computing large-scale budgets and forcing fields. *J. Geophys. Res. Atmos.*, **126**, e2021JD035183, <https://doi.org/10.1029/2021JD035183>.
- Deardorff, J. W., G. E. Willis, and D. K. Lilly, 1969: Laboratory investigation of non-steady penetrative convection. *J. Fluid Mech.*, **35**, 7–31, <https://doi.org/10.1017/S0022112069000942>.
- Del Genio, A. D., Y. Chen, D. Kim, and M.-S. Yao, 2012: The MJO transition from shallow to deep convection in *CloudSat*/CALIPSO and GISS GCM simulations. *J. Climate*, **25**, 3755–3770, <https://doi.org/10.1175/JCLI-D-11-00384.1>.
- DeMott, C. A., N. P. Klingaman, and S. J. Woolnough, 2015: Atmosphere-ocean coupled processes in the Madden–Julian oscillation. *Rev. Geophys.*, **53**, 1099–1154, <https://doi.org/10.1002/2014RG000478>.
- de Szoeke, S. P., and C. S. Bretherton, 2004: Quasi-Lagrangian large eddy simulations of cross-equatorial flow in the East Pacific atmospheric boundary layer. *J. Atmos. Sci.*, **61**, 1837–1858, [https://doi.org/10.1175/1520-0469\(2004\)061%3C1837:QLESOC%3E2.0.CO;2](https://doi.org/10.1175/1520-0469(2004)061%3C1837:QLESOC%3E2.0.CO;2).
- , and E. D. Maloney, 2020: Atmospheric mixed layer convergence from observed MJO sea surface temperature anomalies. *J. Climate*, **33**, 547–558, <https://doi.org/10.1175/JCLI-D-19-0351.1>.
- , J. B. Edson, J. R. Marion, C. W. Fairall, and L. Bariteau, 2015: The MJO and air-sea interaction in TOGA COARE and DYNAMO. *J. Climate*, **28**, 597–622, <https://doi.org/10.1175/JCLI-D-14-00477.1>.
- , E. D. Skillingstad, P. Zuidema, and A. S. Chandra, 2017: Cold pools and their influence on the tropical marine boundary layer. *J. Atmos. Sci.*, **74**, 1149–1168, <https://doi.org/10.1175/JAS-D-16-0264.1>.
- , T. Marke, and W. A. Brewer, 2020: Diurnal ocean surface warming drives convective turbulence and clouds in the atmosphere. *Geophys. Res. Lett.*, **48**, e2020GL091299, <https://doi.org/10.1029/2020GL091299>.
- Feng, Z., S. A. McFarlane, C. Schumacher, S. Ellis, J. Comstock, and N. Bharadwaj, 2014: Constructing a merged cloud-precipitation radar dataset for tropical convective clouds during the DYNAMO/AMIE experiment at Addu Atoll. *J. Atmos. Oceanic Technol.*, **31**, 1021–1042, <https://doi.org/10.1175/JTECH-D-13-00132.1>.
- , S. Hagos, A. K. Rowe, C. D. Burleyson, M. N. Martini, and S. P. de Szoeke, 2015: Mechanism of convective cloud organization by cold pools over tropical warm ocean during the AMIE/DYNAMO field campaign. *J. Adv. Model. Earth Syst.*, **7**, 357–381, <https://doi.org/10.1002/2014MS000384>.
- Gottschalck, J., P. E. Roundy, C. J. Schreck III, A. Vintzileos, and C. Zhang, 2013: Large-scale atmospheric and oceanic conditions during the 2011–12 DYNAMO field campaign. *Mon. Wea. Rev.*, **141**, 4173–4196, <https://doi.org/10.1175/MWR-D-13-00022.1>.
- Haertel, P., K. Straub, and A. Budsock, 2015: Transforming circumnavigating Kelvin waves that initiate and dissipate the Madden–Julian oscillation. *Quart. J. Roy. Meteor. Soc.*, **141**, 1586–1602, <https://doi.org/10.1002/qj.2461>.
- Hayes, S. P., M. J. McPhaden, and J. M. Wallace, 1989: The influence of sea-surface temperature on surface wind in the eastern equatorial Pacific: Weekly to monthly variability. *J. Climate*, **2**, 1500–1506, [https://doi.org/10.1175/1520-0442\(1989\)002<1500:TIOSST>2.0.CO;2](https://doi.org/10.1175/1520-0442(1989)002<1500:TIOSST>2.0.CO;2).
- Hersbach, H., and Coauthors, 2020: The ERA5 global reanalysis. *Quart. J. Roy. Meteor. Soc.*, **146**, 1999–2049, <https://doi.org/10.1002/qj.3803>.
- Huffman, G. J., and Coauthors, 2007: The TRMM multi-satellite precipitation analysis (TMPA): Quasi-global, multi-year, combined-sensor precipitation estimates at fine scale. *J. Hydrometeorol.*, **8**, 38–55, <https://doi.org/10.1175/JHM560.1>.
- Johnson, R. H., and P. E. Ciesielski, 2013: Structure and properties of Madden–Julian oscillations deduced from DYNAMO sounding arrays. *J. Atmos. Sci.*, **70**, 3157–3179, <https://doi.org/10.1175/JAS-D-13-065.1>.
- , and —, 2017: Multiscale variability of the atmospheric boundary layer during DYNAMO. *J. Atmos. Sci.*, **74**, 4003–4021, <https://doi.org/10.1175/JAS-D-17-0182.1>.
- , T. M. Rickenbach, S. A. Rutledge, P. E. Ciesielski, and W. H. Schubert, 1999: Trimodal characteristics of tropical convection. *J. Climate*, **12**, 2397–2418, [https://doi.org/10.1175/1520-0442\(1999\)012%3C2397:TCOTC%3E2.0.CO;2](https://doi.org/10.1175/1520-0442(1999)012%3C2397:TCOTC%3E2.0.CO;2).
- , P. E. Ciesielski, J. H. Ruppert Jr., and M. Katsumata, 2015: Sounding-based thermodynamic budgets for DYNAMO. *J. Atmos. Sci.*, **72**, 598–622, <https://doi.org/10.1175/JAS-D-14-0202.1>.
- Kikuchi, K., and Y. Takayabu, 2003: Equatorial circumnavigation of moisture signal associated with the Madden–Julian Oscillation (MJO) during boreal winter. *J. Meteor. Soc. Japan*, **81**, 851–869, <https://doi.org/10.2151/jmsj.81.851>.
- Klingaman, N. P., and S. J. Woolnough, 2014: The role of air–sea coupling in the simulation of the Madden–Julian oscillation in the Hadley Centre model. *Quart. J. Roy. Meteor. Soc.*, **140**, 2272–2286, <https://doi.org/10.1002/qj.2295>.
- Li, Y., and R. E. Carbone, 2012: Excitation of rainfall over the tropical western Pacific. *J. Atmos. Sci.*, **69**, 2983–2994, <https://doi.org/10.1175/JAS-D-11-0245.1>.
- Lilly, D. K., 1968: Models of cloud-topped mixed layers under a strong inversion. *Quart. J. Roy. Meteor. Soc.*, **94**, 292–309, <https://doi.org/10.1002/qj.49709440106>.
- Lindzen, R. S., and S. Nigam, 1987: On the role of sea surface temperature gradients in forcing low-level winds and convergence in the tropics. *J. Atmos. Sci.*, **44**, 2418–2436, [https://doi.org/10.1175/1520-0469\(1987\)044<2418:OTROSS>2.0.CO;2](https://doi.org/10.1175/1520-0469(1987)044<2418:OTROSS>2.0.CO;2).
- Madden, R. A., and P. R. Julian, 1972: Description of global-scale circulation cells in the tropics with a 40–50 day period. *J. Atmos. Sci.*, **29**, 1109–1123, [https://doi.org/10.1175/1520-0469\(1972\)029<1109:DOGSCC>2.0.CO;2](https://doi.org/10.1175/1520-0469(1972)029<1109:DOGSCC>2.0.CO;2).

- Matthews, A. J., 2008: Primary and successive events in the Madden–Julian Oscillation. *Quart. J. Roy. Meteor. Soc.*, **134**, 439–453, <https://doi.org/10.1002/qj.224>.
- Moteki, Q., 2015: Equatorially antisymmetric features in the initiation processes of the Madden-Julian Oscillation observed in late October during CINDY2011. *J. Meteor. Soc. Japan*, **93A**, 59–79, <https://doi.org/10.2151/jmsj.2015-040>.
- Moulin, A. J., J. N. Moum, and E. L. Shroyer, 2018: Evolution of turbulence in the diurnal warm layer. *J. Phys. Oceanogr.*, **48**, 383–396, <https://doi.org/10.1175/JPO-D-17-0170.1>.
- Moum, J. N., and Coauthors, 2014: Air–sea interactions from westerly wind bursts during the November 2011 MJO in the Indian Ocean. *Bull. Amer. Meteor. Soc.*, **95**, 1185–1199, <https://doi.org/10.1175/BAMS-D-12-00225.1>.
- Powell, S. W., 2016: Updraft buoyancy within and moistening by cumulonimbus prior to MJO convective onset in a regional model. *J. Atmos. Sci.*, **73**, 2913–2934, <https://doi.org/10.1175/JAS-D-15-0326.1>.
- , 2017: Successive MJO propagation in MERRA-2 reanalysis. *Geophys. Res. Lett.*, **44**, 5178–5186, <https://doi.org/10.1002/2017GL073399>.
- , and R. A. Houze Jr., 2015a: Effect of dry large-scale vertical motions on initial MJO convective onset. *J. Geophys. Res. Atmos.*, **120**, 4783–4805, <https://doi.org/10.1002/2014JD022961>.
- , and —, 2015b: Evolution of precipitation and convective echo top heights observed by TRMM radar over the Indian Ocean during DYNAMO. *J. Geophys. Res. Atmos.*, **120**, 3906–3919, <https://doi.org/10.1002/2014JD022934>.
- Rowe, A. K., and R. A. Houze Jr., 2015: Cloud organization and growth during the transition from suppressed to active MJO conditions. *J. Geophys. Res. Atmos.*, **120**, 10 324–10 350, <https://doi.org/10.1002/2014JD022948>.
- Ruppert, J. H., Jr., 2016: Diurnal timescale feedbacks in the tropical cumulus regime. *J. Adv. Model. Earth Syst.*, **8**, 1483–1500, <https://doi.org/10.1002/2016MS000713>.
- Ruppert, J. H. Jr., and R. H. Johnson, 2015: Diurnally modulated cumulus moistening in the preonset stage of the Madden–Julian oscillation during DYNAMO. *J. Atmos. Sci.*, **72**, 1622–1647, <https://doi.org/10.1175/JAS-D-14-0218.1>.
- Ruppert, J. H., Jr., and R. H. Johnson, 2016: On the cumulus diurnal cycle over the tropical warm pool. *J. Adv. Model. Earth Syst.*, **8**, 669–690, <https://doi.org/10.1002/2015MS000610>.
- Rydbeck, A. V., T. G. Jensen, and E. S. Nyadjro, 2017: Intraseasonal sea surface warming in the western Indian Ocean by oceanic equatorial Rossby waves. *Geophys. Res. Lett.*, **44**, 4224–4232, <https://doi.org/10.1002/2017GL073331>.
- Samelson, R. M., E. D. Skvillingstad, D. B. Chelton, S. K. Esbensen, L. W. O’Neill, and N. Thum, 2006: On the coupling of wind stress and sea surface temperature. *J. Climate*, **19**, 1557–1566, <https://doi.org/10.1175/JCLI3682.1>.
- Schubert, W. H., J. S. Wakefield, E. J. Steiner, and S. K. Cox, 1979: Marine stratocumulus convection. Part II: Horizontally inhomogeneous solutions. *J. Atmos. Sci.*, **36**, 1308–1324, [https://doi.org/10.1175/1520-0469\(1979\)036<1308:MSCPIH>2.0.CO;2](https://doi.org/10.1175/1520-0469(1979)036<1308:MSCPIH>2.0.CO;2).
- Shell, K. M., S. P. de Zoete, M. Makiyama, and Z. Feng, 2020: Vertical structure of radiative heating rates of the MJO during DYNAMO. *J. Climate*, **33**, 5317–5335, <https://doi.org/10.1175/JCLI-D-19-0519.1>.
- Small, R. J., and Coauthors, 2008: Air–sea interaction over ocean fronts and eddies. *Dyn. Atmos. Oceans*, **45**, 274–319, <https://doi.org/10.1016/j.dynatmoce.2008.01.001>.
- Snide, C. E., Á. F. Adames, S. W. Powell, and V. C. Mayta, 2021: The role of large-scale moistening by adiabatic lifting in the Madden–Julian oscillation convective onset. *J. Climate*, **35**, 269–284, <https://doi.org/10.1175/JCLI-D-21-0322.1>.
- Vialard, J., and Coauthors, 2009: Cirene: Air–sea interactions in the Seychelles–Chagos thermocline ridge region. *Bull. Amer. Meteor. Soc.*, **90**, 45–62, <https://doi.org/10.1175/2008BAMS2499.1>.
- Virts, K. S., and J. M. Wallace, 2010: Annual, interannual, and intraseasonal variability of tropical tropopause transition layer cirrus. *J. Atmos. Sci.*, **67**, 3097–3112, <https://doi.org/10.1175/2010JAS3413.1>.
- Wallace, J. M., T. P. Mitchell, and C. Deser, 1989: The influence of sea-surface temperature on surface wind in the eastern equatorial Pacific: Seasonal and interannual variability. *J. Climate*, **2**, 1492–1499, [https://doi.org/10.1175/1520-0442\(1989\)002<1492:TIOSSST>2.0.CO;2](https://doi.org/10.1175/1520-0442(1989)002<1492:TIOSSST>2.0.CO;2).
- Weller, R. A., and S. P. Anderson, 1996: Surface meteorology and air–sea fluxes in the western equatorial Pacific warm pool during the TOGA coupled ocean–atmosphere response experiment. *J. Climate*, **9**, 1959–1990, [https://doi.org/10.1175/1520-0442\(1996\)009<1959:SMAASF>2.0.CO;2](https://doi.org/10.1175/1520-0442(1996)009<1959:SMAASF>2.0.CO;2).
- Wheeler, M. C., and H. H. Hendon, 2004: An all-season real-time multivariate MJO index: Development of an index for monitoring and prediction. *Mon. Wea. Rev.*, **132**, 1917–1932, [https://doi.org/10.1175/1520-0493\(2004\)132<1917:AARMMI>2.0.CO;2](https://doi.org/10.1175/1520-0493(2004)132<1917:AARMMI>2.0.CO;2).
- Wielicki, B. A., B. R. Barkstrom, E. F. Harrison, R. B. Lee III, G. L. Smith, and J. E. Cooper, 1996: Clouds and the Earth’s Radiant Energy System (CERES): An Earth observing system experiment. *Bull. Amer. Meteor. Soc.*, **77**, 853–868, [https://doi.org/10.1175/1520-0477\(1996\)077<0853:CATERE>2.0.CO;2](https://doi.org/10.1175/1520-0477(1996)077<0853:CATERE>2.0.CO;2).
- Wu, J., Y. Li, J.-J. Luo, and X. Jiang, 2021: Assessing the role of air–sea coupling in predicting Madden–Julian oscillation with an atmosphere–ocean coupled model. *J. Climate*, **34**, 9647–9663, <https://doi.org/10.1175/JCLI-D-20-0989.1>.
- Xu, W., and S. A. Rutledge, 2014: Convective characteristics of the Madden–Julian oscillation over the central Indian Ocean observed by shipborne radar during DYNAMO. *J. Atmos. Sci.*, **71**, 2859–2877, <https://doi.org/10.1175/JAS-D-13-0372.1>.
- Yoneyama, K., C. Zhang, and C. N. Long, 2013: Tracking pulses of the Madden–Julian oscillation. *Bull. Amer. Meteor. Soc.*, **94**, 1871–1891, <https://doi.org/10.1175/BAMS-D-12-00157.1>.
- Yu, L., and R. A. Weller, 2007: Objectively analyzed air–sea heat fluxes for the global ice-free oceans (1981–2005). *Bull. Amer. Meteor. Soc.*, **88**, 527–540, <https://doi.org/10.1175/BAMS-88-4-527>.
- Zhang, C., J. Gottschalck, E. D. Maloney, M. W. Moncrieff, F. Vitart, D. E. Waliser, B. Wang, and M. C. Wheeler, 2013: Cracking the MJO nut. *Geophys. Res. Lett.*, **40**, 1223–1230, <https://doi.org/10.1002/grl.50244>.
- Zhang, F., S. Taraphdar, and S. Wang, 2017: The role of global circumnavigating mode in the MJO initiation and propagation. *J. Geophys. Res. Atmos.*, **122**, 5837–5856, <https://doi.org/10.1002/2016JD025665>.
- Zuidema, P., G. Torri, C. Muller, and A. Chandra, 2017: A survey of precipitation-induced atmospheric cold pools over oceans and their interactions with the larger-scale environment. *Surv. Geophys.*, **38**, 1283–1305, <https://doi.org/10.1007/s10712-017-9447-x>.